Structured abstract

- **Purpose**

  In order to understand the behaviour of magnetization processes in ferromagnetic materials in function of temperature, a temperature-dependent hysteresis model is necessary. This article investigates how temperature can be accounted for in the Energy-Based hysteresis model, via an appropriate parameter identification and interpolation procedure.

- **Design/methodology/approach**

  The hysteresis model used for simulating the material response is energy-consistent and relies on thermodynamic principles. The material parameters have been identified by unidirectional alternating measurements and the model has been tested for both simple and complex excitation waveforms. Measurements and simulations have been performed on a soft ferrite toroidal sample characterized in a wide temperature range.

- **Findings**

  The analysis shows that the model is able to represent accurately arbitrary excitation waveforms in function of temperature. The identification method used to determine the model parameters has proven its robustness: starting from simple excitation waveforms, the complex ones can be simulated precisely.

- **Research limitations/implications**

  As parameters vary depending on temperature, a new parameter variation law in function of temperature has been proposed.

- **Practical implications**

  A complete static hysteresis model able to take the temperature into account is now available. The identification is quite simple and requires very few measurements at different temperatures.

- **Originality/value**

  Results suggest that it is possible to predict magnetization curves within the measured range starting from a reduced set of measured data.

1 Introduction

The growing demand for components to operate under extreme conditions [Cass et al., 2007] motivates the analysis of the effect of temperature variations on magnetic materials, in particular soft magnetic materials at high temperatures. Currently available soft magnetic materials are required to cover a wide spectrum of applications, from cores of transformers and motors to the extensive variety of inductive components used in power electronics, automotive and household technologies. Soft magnetic materials used in power electronics, such as MnZn ferrites, are strongly dependent on temperature because of their low Curie temperature ($T_c \geq 493$ K) [Fer, 2013]. Thus, designers need models able to predict the behaviour of such materials in a large temperature range. For engineering applications, the main driving forces are the ability to reproduce the hysteresis curves and to calculate related energy losses due to magnetization processes. Determining such effects in complex geometries requires the use of numerical methods such as the Finite Element method, where the inclusion of material laws need to be computationally efficient and should ideally enable the simulation of arbitrary waveforms at any temperature. A number of authors have proposed strategies to take into account temperature in conventional hysteresis models, such as Preisach [Preisach, 1935], [Preisach, 2017], [Stancu and Spinu, 1998], [Song and Roshko, 2000] or the Jiles-Atherton (JA) [Jiles and Atherton, 1986], [Raghunathan et al., 2010]. The Preisach model focuses on a mathematical description of the hysteresis property and reproduces magnetization curves accurately, but mostly ignores the underlying physics of the magnetic material. The JA model generally fails to predict accurately excitation fields for complex magnetization waveforms [Benabou et al., 2008], [Petrun et al., 2017], due to several intrinsic drawbacks detailed in [Zirka et al., 2012]. Among the existing alternative hysteresis models, the Energy-Based (EB) model [Bergqvist, 1997], [Henrotte et al., 2006], [François-Lavet et al., 2011], [Henrotte et al., 2014] has many advantages. Particularly, it relies on thermodynamic principles and it is energy-consistent. This is extremely interesting for engineers, who need hysteresis models based on physical foundations, able to take into account both complex excitation waveforms and the influence of temperature on magnetic properties [Bergqvist et al., 2014]. In this work, we present recent developments on the dependence of the EB model on temperature, and propose a new parameter variation law in function of temperature for soft ferrites. The hysteresis model is validated through measurements, in case of both simple (unidirectional alternating measurements) and complex (unidirectional with addition of harmonics) excitation waveforms in order to explore its prediction of arbitrary magnetization curves at any temperature. The objective of temperature-dependent model is twofold: 1) to

predict the device performance at a given external temperature; and 2) to determine the equilibrium temperature for a given operating mode, in a specific operating environment, in order to optimize components in their design phase.

2 Methods

2.1 Experimental setup

Figure 1 illustrates the experimental setup for measuring magnetic hysteresis loops using ring sample. A thermal chamber is used for measurements at different temperatures. The sample is a toroidal core made of soft ferrite MnZn 3C90 [Fer, 2013] with primary and secondary windings (Table 1). Excitation is applied using an arbitrary function generator which allows to impose current on the primary winding. By means of the Ampere (1) and Faraday laws (2), the magnetic field h and the magnetic flux density b are calculated from the measurements of the current in the primary winding and the voltage on the secondary winding:

$$h(t) = \frac{N_1 \cdot V_{shunt}(t)}{R_{shunt} \cdot l_e} \tag{1}$$

$$b(t) = -\frac{1}{N_2 \cdot A_e} \int V_2(t) \cdot dt \tag{2}$$

The EB model is validated against experimental data of 3C90 material. The hysteresis loops have been measured using the experimental setup at various temperatures (223 K, 248 K, 273 K, 293 K, 323 K, 348 K, 373 K, 398 K, 423 K and 448 K) and compared with those calculated numerically.

Table 1: Symbols and description of each quantity.

Symbol	**Value**	**Description**
N_1	60	primary winding
N_2	39	secondary winding
R_{shunt}	2 Ω	shunt resistance
R_s	176 Ω	series resistance
l_e	73.2 mm	effective magnetic path length of the core
A_e	36.9 mm^2	effective cross-sectional area of the core

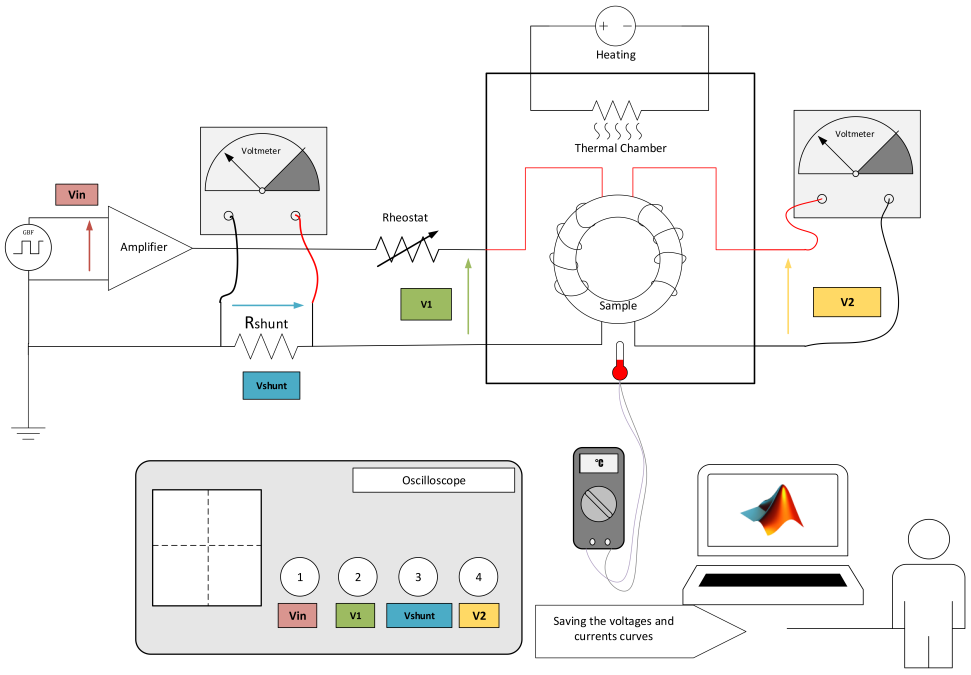

Figure 1: System for measuring magnetic hysteresis loops $b(h)$.

2.2 The Energy-Based hysteresis model

2.2.1 Thermodynamic basis

The model relies on thermodynamic foundation to represent the nonlinear behaviour of ferromagnetic material [Bergqvist, 1997], [Henrotte et al., 2006], [François-Lavet et al., 2011], [Henrotte et al., 2014]. The first law of thermodynamics expresses the conservation of energy:

$$\dot{u} = \mathbf{h} \cdot \dot{\mathbf{J}} - D, \qquad \mathbf{J} = \mathbf{b} - \mu_0 \mathbf{h} \tag{3}$$

where u is the magnetic energy density stored in the material, D is a dissipation functional which will be defined more precisely thereafter, $\mathbf{h}\cdot\dot{\mathbf{J}}$ is the magnetic external work, with $\mathbf{h}$ corresponding to the applied magnetic field, $\mathbf{J}$ the magnetic polarization of the material, $\mathbf{b}$ the magnetic flux density and μ_0 the permeability of vacuum[1]. The model is based on a mechanical analogy, where the input is the magnetic field $\mathbf{h}$. The magnetic field can be decomposed in a *reversible part* $\mathbf{h}_r$ and an *irreversible part* $\mathbf{h}_{ir}$:

$$\mathbf{h} = \mathbf{h}_r + \mathbf{h}_{ir} \tag{4}$$

acting respectively as spring force and friction force [Henrotte et al., 2006]. The energy density u is assumed to be a function of $\mathbf{J}$,

$$u = u(\mathbf{J}) \qquad \Rightarrow \qquad \dot{u} = \left(\frac{\partial u}{\partial \mathbf{J}}\right) \cdot \dot{\mathbf{J}} = \mathbf{h}_r \cdot \dot{\mathbf{J}} \tag{5}$$

[1]The notation $\dot{\square} = \partial/\partial t$ means time derivative (example: $\dot{u} = \partial u/\partial t$).

where the term $\mathbf{h}_r$ is called reversible part of the magnetic field, in that the magnetic work it delivers under a variation of the magnetic polarization is fully converted into internal energy. Hysteresis in ferromagnetic materials can be interpreted physically as defects at microscopical scale. Defects pin domain walls and prevent them from moving under the effect of an external magnetic field. When the material is magnetized or demagnetized, the walls suddenly rearrange and jump abruptly from one pinning site to the next one, hence the (irreversible) hysteresis behavior. By using (4) and (5) in (3), the dissipation functional D associated with the dry-friction force writes:

$$D = \mathbf{h}_{ir} \cdot \dot{\mathbf{J}} = \kappa \left|\dot{\mathbf{J}}\right| \qquad \Rightarrow \qquad \mathbf{h}_{ir} = \frac{\partial D}{\partial \dot{\mathbf{J}}} = \kappa \frac{\dot{\mathbf{J}}}{\left|\dot{\mathbf{J}}\right|} \tag{6}$$

where κ in A/m is a material characteristic called *pinning field*, that opposes the motion of domains walls. It is proportional to the pinning site energy that determines the coercivity h_c of the hysteresis loop. Hence, the dissipation D is the power delivered by the irreversible magnetic field $\mathbf{h}_{ir}$. Combining (3)-(6) provides the following equation:

$$\mathbf{h} - \mathbf{h}_r - \mathbf{h}_{ir} = 0 \qquad \Rightarrow \qquad \mathbf{h} - \frac{\partial u}{\partial \mathbf{J}} - \kappa \frac{\dot{\mathbf{J}}}{\left|\dot{\mathbf{J}}\right|} = 0 \tag{7}$$

Since the functional D is not differentiable in $\dot{\mathbf{J}} = 0$, $\mathbf{h}_{ir}$ can be defined by means of a *subgradient* of the functional D:

$$\mathbf{h}_{ir} \in \left\{ \mathbf{h}_{ir}, |\mathbf{h}_{ir}| \leq \kappa \;\text{ if }\; \dot{\mathbf{J}} = 0, \quad \mathbf{h}_{ir} = \kappa \frac{\dot{\mathbf{J}}}{\left|\dot{\mathbf{J}}\right|} \;\text{ otherwise} \right\} \tag{8}$$

2.2.2 Two-scale model

Real ferromagnetic materials are characterized by a statistical distribution of pinning fields [Bergqvist, 1997], [Bergqvist et al., 1997], [Henrotte et al., 2014]. For this reason, a multi-scale model has been elaborated. It relies on the fact that the material, homogeneous at the macroscopic scale, is composed of N heterogeneous microscopic abstract subregions (also called *cells*), defined by a specific pinning force κ^k. The reversible magnetic field $\mathbf{h}_r$ is computed as the weighted sum of contributions $\mathbf{h}_r^k$ of a number of cells N (9):

$$\mathbf{h}_r = \sum_{k=1}^{N} \omega_k \mathbf{h}_r^k \tag{9}$$

In this sum, ω_k are the weights associated to cells, namely they highlights the relative importance of each contribution and must verify the condition $\sum_{k=1}^{N} \omega_k = 1$. Basing on the knowledge of the magnetic field $\mathbf{h}$, independent equations can be solved for each cell:

$$\mathbf{h} - \mathbf{h}_r^k - \mathbf{h}_{ir}^k = 0 \qquad \Rightarrow \qquad \mathbf{h} - \frac{\partial u^k}{\partial \mathbf{J}^k} - \kappa^k \frac{\dot{\mathbf{J}^k}}{\left|\dot{\mathbf{J}^k}\right|} = 0 \tag{10}$$

The number of cells in which the EB model is discretized depends on the required accuracy: models with higher number of cells will be more accurate, but also more complex to handle from the computational point of view. The resolution of the non-linear differential equations (10) is proposed in [Henrotte et al., 2006]. An approximate solution is obtained on the basis of the explicit update rule, in which the terms $\mathbf{h}_r^k$ are upgraded as a function of the applied magnetic field $\mathbf{h}$ and of their previous value $\mathbf{h}_{r0}^k$ according to:

$$\mathbf{h}_r^k = \begin{cases} \mathbf{h}_{r0}^k & \text{if } \left|\mathbf{h} - \mathbf{h}_{r0}^k\right| < \kappa^k \\ \mathbf{h} - \kappa^k \cdot \frac{\mathbf{h}-\mathbf{h}_{r0}^k}{\left|\mathbf{h}-\mathbf{h}_{r0}^k\right|} & \text{otherwise} \end{cases} \tag{11}$$

In Figure 2 a visual representation of the update rule is shown. The sphere of radius κ centered in $\mathbf{h}_r$ represents the subgradient (8). Equation (7) imposes that the tip of applied magnetic field $\mathbf{h}$ is either inside the sphere or on its surface. If the tip of $\mathbf{h}$ moves inside the sphere, then the condition

$$\left|\mathbf{h} - \mathbf{h}_{r0}^k\right| < \kappa^k \tag{12}$$

is fulfilled and the sphere remains fixed. If $\mathbf{h}$ tends to go beyond the sphere, the latter has to shift to comply with the condition (12), i.e. the center of the sphere moves according to (11). Since $\mathbf{J} = \mu_0\mathbf{M}$, the magnetization is computed thanks to (13):

$$\mathbf{M} = M_{an}(|\mathbf{h}_r|)\frac{\mathbf{h}_r}{|\mathbf{h}_r|} \tag{13}$$

where M_{an} is a scalar, monotone increasing anhysteretic magnetization function. Finally, the magnetic flux density is computed as:

$$\mathbf{b} = \mu_0(\mathbf{M} + \mathbf{h}) \tag{14}$$

The present model is completely characterized by the anhysteretic curve M_{an} and

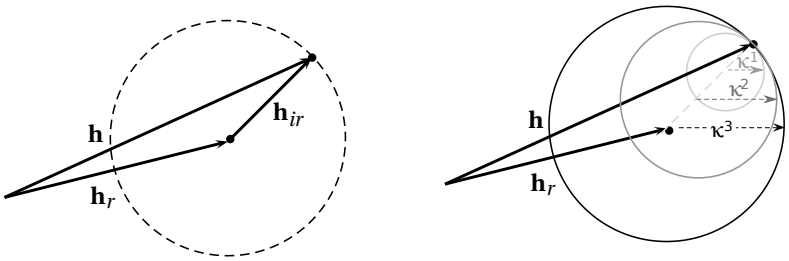

Figure 2: Vector diagram of $\mathbf{h} = \mathbf{h}_r + \mathbf{h}_{ir}$ for $N = 1$ (left) and $N = 3$ cells (right), adapted from [Sixdenier and Scorretti, 2018].

by the couples of parameters $(\omega_k, \kappa^k)_{k=1\ldots N}$. M_{an} can be represented by analytical expressions, i.e. Langevin or double Langevin functions [Henrotte et al., 2006] or

interpolated from experimental measurements [Sixdenier and Scorretti, 2018]. Thus, the major loop is measured at several temperatures and $M_{an}(h,T)$ is computed by considering the median line of the major loop. Then, the anhysteretic function $M_{an}(h,T)$ for any value of h and T is obtained by 2D interpolation.

2.3 Parameters identification

The discrete parameters ω_k and κ^k must verify the following constraints:

$$\omega_k \geq 0 \quad ; \quad \sum_{k=1}^{N} \omega_k = 1 \tag{15}$$

$$\kappa^1 = 0 \quad ; \quad \kappa^k \leq \kappa^{k+1} \tag{16}$$

In order to identify the material coefficients $(\omega_k, \kappa^k)_{k=1...N}$, it has been proposed [Jacques et al., 2018] to determine the pinning field probability density $\omega(\kappa)$. For a given temperature, the identification procedure relies on a set of hysteresis loops measured in unidirectional conditions. It focuses on the experimental curve $h_c(h_p)$ obtained from the measurement of a series of hysteresis loops of increasing amplitude h_p. The coercive field h_c is detected on a cycle, for which the applied magnetic field amplitude is h_p. The $h_c(h_p)$ characteristic is interpolated in the range $[h_{p_{min}}, h_{p_{max}}]$ and it is extrapolated as follow for field values outside the measurement range (17):

$$h_c(h_p) = \begin{cases} h_c = h_{c_{max}} & \text{if } h_p > h_{p_{max}} \\ h_c = f(h_p) & \text{if } h_{p_{min}} < h_p < h_{p_{max}} \\ h_c = h_{c_{min}} \cdot \left(\frac{h_p}{h_{p_{min}}}\right)^2 & \text{if } h_p < h_{p_{min}} \end{cases} \tag{17}$$

where $f(h_p)$ is an interpolation function[2]. The quadratic extrapolation at low fields derives from Rayleigh law [Rayleigh, 1887]. The next step is the definition of an auxiliary continuous function $F(h)$, based on the $h_c(h_p)$ curve. The curve $h_c(h_p)$ contains enough information to completely identify $F(h)$ [Jacques et al., 2018]. For any magnetic field h which saturates the material ($h > h_{p_{max}}$) it is known that:

$$F(h) = h - h_{c_{max}} \tag{18}$$

For magnetic fields of lower magnitude, the function F satisfies:

$$F\left(\frac{h + h_c(h)}{2}\right) = \frac{F(h)}{2} \tag{19}$$

The procedure consists in selecting an arbitrary initial value $h^0 > h_{p_{max}}$. The subsequent terms of the series are recursively given by:

$$h^n = \frac{h^{n-1} + h_c(h^{n-1})}{2} \tag{20}$$

[2]In principle, any interpolation method can be used. We used piecewise linear interpolation because this method ensures that no unphysical negative values are obtained.

The values of function $F(h^n)$ can then be computed as:

$$F(h^n) = \begin{cases} h^n - h_{c_{max}} & \text{if } h^n > h_{p_{max}} \\ \frac{F(h^{n-1})}{2} & \text{otherwise} \end{cases} \tag{21}$$

By using (18)-(21), the curve $F(h)$ can be sampled in an arbitrary number of points. The pinning field (continuous) probability density $\omega(\kappa)$ is then deduced by derivating $F(h)$ twice:

$$\omega(\kappa) = \frac{\partial^2 F(h)}{\partial h^2}$$

By using this procedure, the continuous distribution $\omega(\kappa)$ can be numerically computed in a very high number of points. In practice, a discrete approximation of the distribution $\omega(\kappa)$ is needed for Finite Element implementations [Henrotte et al., 2014]. For this reason, the discrete sets of parameters $(\omega_k, \kappa^k)_{k=1,\dots,N}$ are derived from the continuous distributions $\omega(\kappa)$ previously obtained, where the number N of cells is much lower (tipically $N \leq 10$).

3 Results

3.1 Experimental measurements

The EB model has been evaluated by comparing the simulated and measured hysteresis loops for the ferrite 3C90 material. Experimental hysteresis loops have been measured in differents conditions:

- simple excitation waveforms:
  - *variable-temperature*: sinusoidal excitation waveform ($f = 50$ Hz), T ranging from 223 to 448 K, $h_p = const$ (Figure 3 for $h_p = 230$ A/m).
  - *variable-amplitude*: sinusoidal excitation waveform ($f = 50$ Hz), h_p ranging from 20 to 230 A/m, $T = const$ (Figure 3 for $T = 293$ K).
- complex excitation waveforms:
  - sinusoidal excitation waveform ($f = 50$ Hz) with superimposed higher harmonic ($f = 150$ Hz) for different levels of h_{max}, $T = 293$ K (Figure 4a):

$$h(t) = h_{max}(\sin(2\pi f t) + \sin(6\pi f t)) \tag{22}$$

  - pulse-width modulation (PWM) excitation (fundamental $f = 1$ kHz with addition of 3rd and 7th harmonics) at $T = 323$ K (Figure 4b) and $T = 373$ K (not shown).

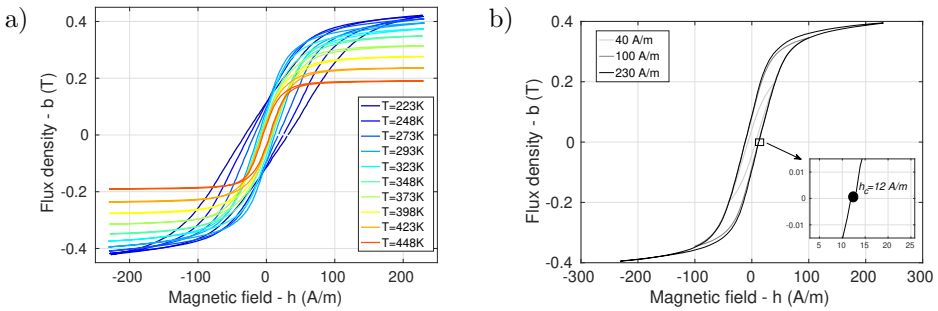

Figure 3: Simple excitation waveforms: (a) measurements at $h_p = 230$ A/m in the temperature range, (b) Measurements at $T = 293$ K and $h_p = 40$ A/m, 100 A/m, 230 A/m (zoom: coercive field $h_c = 12$ A/m related to the cycle for which $h_p = 230$ A/m).

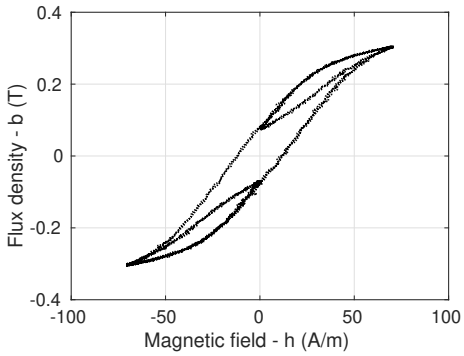

(a) Measured loop at $T = 293$ K with superimposed 3rd harmonic component to the fundamental.

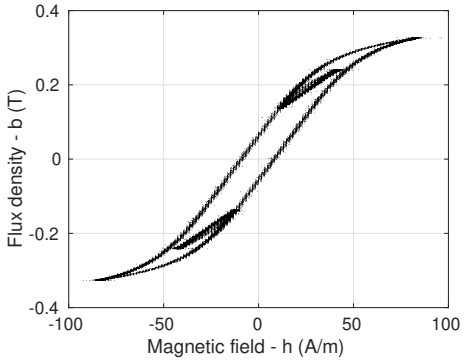

(b) Measured loop with PWM excitation at $T = 323$ K.

Figure 4: Complex excitation waveforms.

3.2 Parameters identification

The protocol previously described has been applied to 3C90 ferrite in the measured temperature range. The $h_c(h_p)$ characteristics have been measured for each series

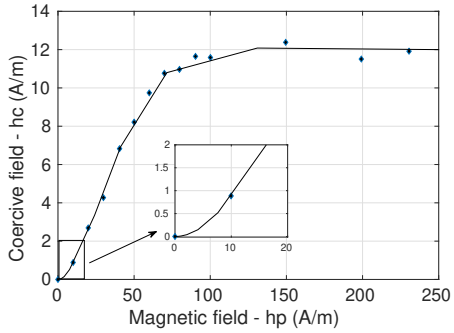

(a) Curve $h_c(h_p)$ for 3C90 material ($T = 293$ K).

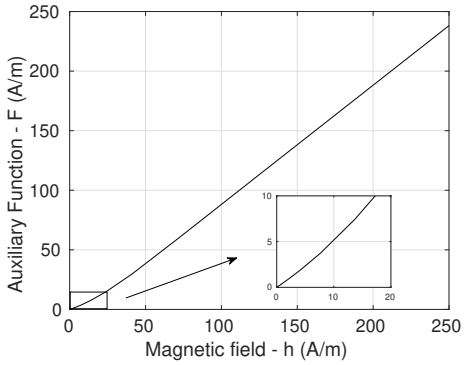

(b) Auxiliary function $F(h)$ ($T = 293$ K).

Figure 5: Identification procedure.

of hysteresis loops of increasing h_p, for each temperature. As an example, in Figure 5 we show the construction of the curve $h_c(h_p)$ (Fig. 5a) and the corresponding auxiliary function $F(h)$ (Fig. 5b) at the temperature $T = 293$ K. The variation of the $h_c(h_p)$ curves in function of temperature is shown in Figure 6a. We observe that the coercive field decreases as temperature raises, which is coherent with the cycles depicted in Figure 3. Figure 6b depicts the estimated continuous distributions $\omega(\kappa|T)$.

One observes that the average pinning field decreases, as the temperature increases. This could be explained by the fact that for higher temperatures, thermal noise makes easier to overcome pinning energy barriers, and therefore reduces the pinning field. On the other hand, it is reported in literature [Raghavender et al., 2010] that at the higher temperatures grain size increases. Therefore, the growth of grain size increases the distance of pinning points in the material and, consequently, decreases

the coercive field.

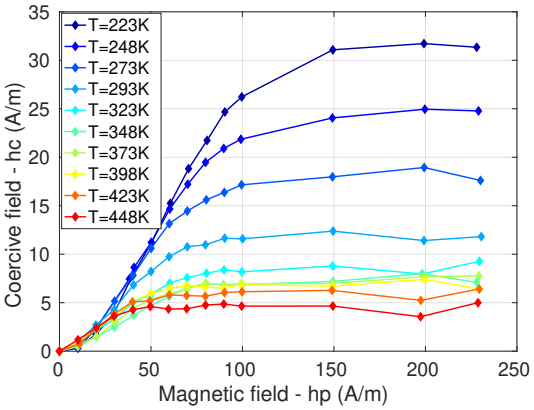

(a) Curve $h_c(h_p)$ for 3C90 material in the temperature range.

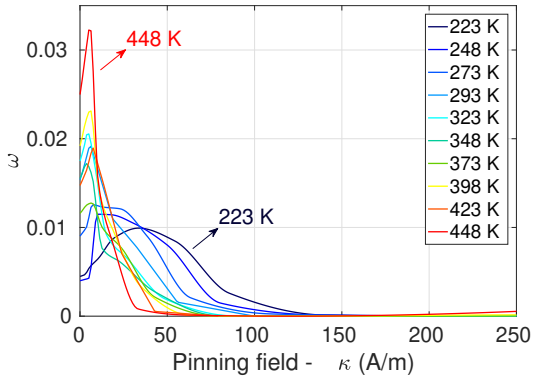

(b) Continuous distributions $\omega(\kappa|T)$.

Figure 6: Variation of parameters in function of temperature.

3.3 Various tests of the EB model

We tested the EB model with several kinds of signals and temperatures, by varying the number of cells from 2 to 8. Results are shown in Figures 7-8-9.

3.3.1 Major loops

In Figure 7, simulations with $N = 3$ cells reproduce major loops at different temperatures and amplitudes:

- Figure 7a compares measured and simulated $b(h)$ loops with the same amplitude ($h_p = 230$ A/m) for different temperatures ($T = 248$ K, $T = 348$ K and $T = 448$ K).

- Figure 7b compares measured and simulated curves with different amplitudes ($h_p = 40$ A/m, $h_p = 100$ A/m and $h_p = 230$ A/m) at the same temperature ($T = 293$ K).

The precision of the EB model in predicting the measured cycles has been quantified by means of the relative normalized root mean square error (NRMSE) between simulated and measured flux density:

$$\text{NRMSE} = \frac{\sqrt{\sum_{n=1}^{N_{meas}} ||b_{sim,n} - b_{meas,n}||^2}}{\sqrt{\sum_{n=1}^{N_{meas}} ||b_{meas,n}||^2}} \times 100\% \tag{23}$$

where N_{meas} is the number of measurement points. Figure 9 depicts the NRMSE for a number of cells spanning from 2 to 8:

- Figure 9a represents the NRMSE as a function of temperature, for cycles of fixed amplitude $h_p = 230$ A/m (cf. Fig. 7a).
- Figure 9b represents the NRMSE as a function of cycle amplitude, for a fixed temperature $T = 293$ K (cf. Fig. 7b).

It is observed that for major cycles, a quite good representation of hysteresis loops (NRMSE $< 5\%$) is generally obtained starting from 3 cells. For cycles of lower amplitudes (Fig. 9b) results are mixed. The global trend is that the error is proportionally lower for cycles of higher amplitude. This can be explained by the argument that for cycles of high amplitude, all cells are activated simultaneously. Moreover, when the material is saturated, the field is determined by the saturation value of M_{an} more than by the exact value of h_r. Conversely, at low fields not all cells are activated, and thus the details of (ω_k, κ^k) play a much more important role. Nevertheless, the NRMSE stabilizes for $N \geq 3$, apart from very low-amplitude cycles ($h_p \leq 30$ A/m) for which a higher number of cells can be used in order to increase the accuracy. The fact that the error is particularly low in the case $h_p = 30$ A/m is unexplained, and it is likely to be a particular case.

3.3.2 Complex signals

The same identified parameters have been employed to simulate complex magnetization trajectories. The model can effectively simulate signals with harmonics (closed small loops at the tips of each loop) at a given temperature. Measurements have been performed for $T = 293$ K, $T = 323$ K and $T = 373$ K. The cycles measured and simulated with $N = 4$ cells for $T = 293$ K are depicted in Figure 8a. Figure 8b depicts the NRMSE for each temperature. It can be observed that EB model produces stable minor loops, namely it closes the loops in a physically adequate

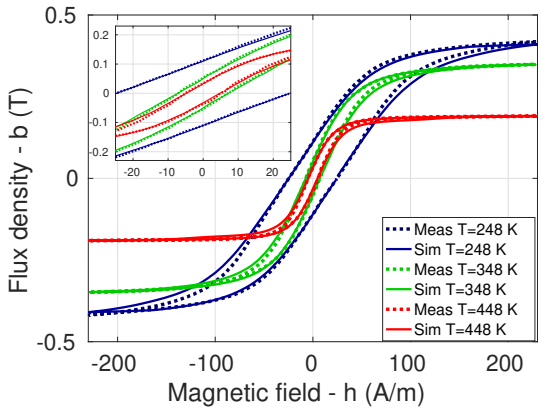

(a) Measured and simulated major loops at h_p = 230 A/m for different temperatures (248 K, 348 K, 448 K) with $N = 3$ cells.

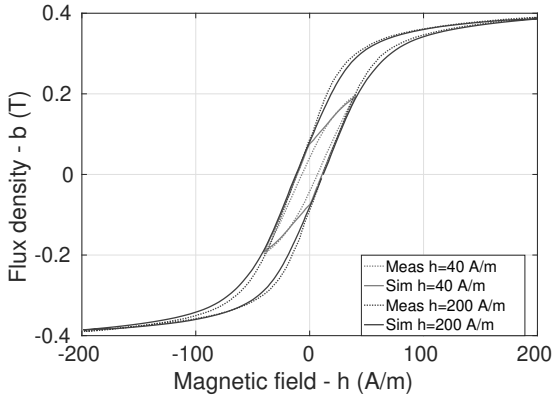

(b) Variation of hysteresis loop with magnetic field intensity, $h_p = 40$ A/m and $h_p = 200$ A/m, with $N = 3$ cells ($T = 293$ K).

Figure 7: Simulated and measured loops for simple excitation waveforms. Dotted lines: measured values; full lines: simulated values.

manner, conversely to the original JA model [Benabou et al., 2008], [Zirka et al., 2012], [Petrun et al., 2017]. Note that the model has been applied with the same parameters identified with simple (sinusoidal) excitation waveforms. Simulated and measured results are globally in good agreement, showing that the model is able to predict complex loops at any temperature, at least within the measured range.

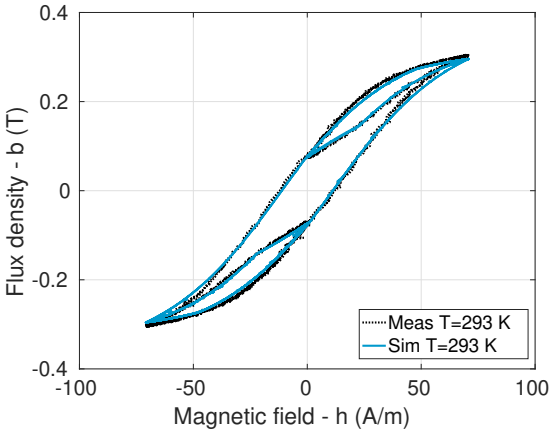

(a) Loops with third harmonic at $T = 293$ K.

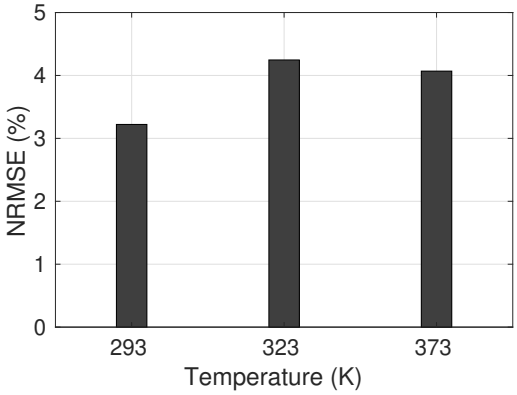

(b) NRMSE for complex excitation waveforms at 293 K, 323 K and 373 K.

Figure 8: Simulated/measured loops and NRMSE for complex excitation waveforms at different temperatures ($N = 4$ cells).

4 Discussion

This study puts in evidence how the distribution of pinning field $\omega(\kappa)$ depends on the temperature T. The observed trend is that the peak of the distribution shifts towards lower values when the temperature increases (Fig. 6b). This evidence could be explained by the argument that higher thermal noise reduces the energy required

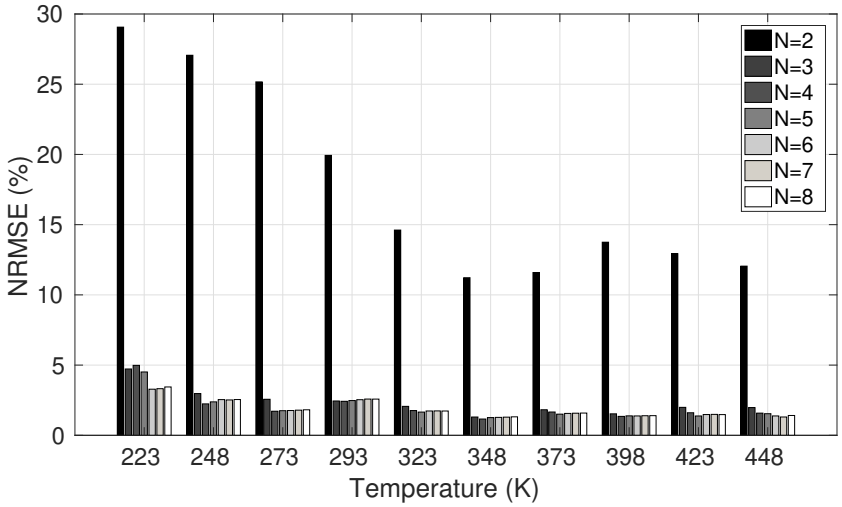

(a) NRMSE at constant amplitude of applied field ($h_p = 230$ A/m) for different temperatures by varying the number of cells N.

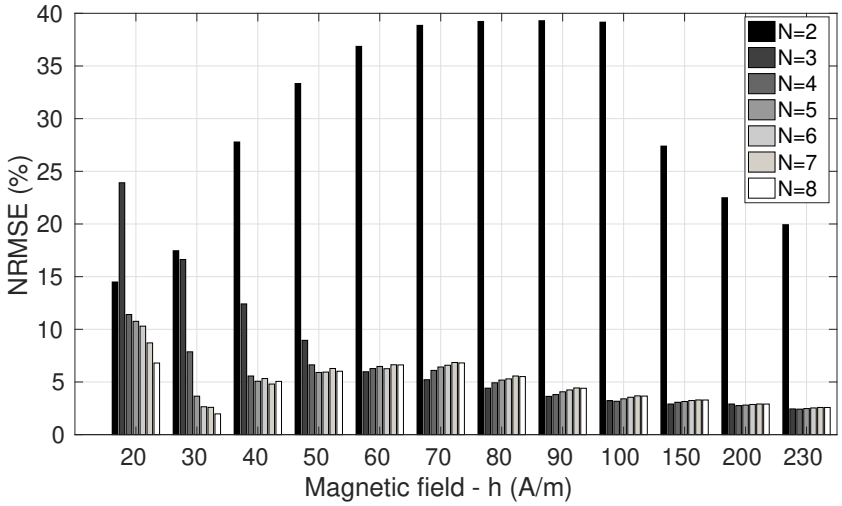

(b) NRMSE at different levels of applied field ($T = 293$ K) by varying the number of cells N.

Figure 9: Quantitative evaluation of errors between measurements and simulations.

to overcome pinning energy barriers.

From the analysis of the precision of the model, it is observed that the NRMSE is generally higher for low temperature (Fig. 9a) and/or for low applied field (Fig. 9b). These two facts could be linked, in that under low thermal noise and/or low applied field, cells corresponding to low pinning field are not simultaneously activated[3], and therefore the material exhibits a more complex behaviour.

[3]Cells which activate simultaneously are practically indistinguishable. This fact has been used in [Sixdenier and Scorretti, 2018] to build simplified EB models.

Figure 7a compares calculated and experimental loops for three temperatures (248 K, 348 K, 448 K). In the case of $T = 248$ K it has been impossible to completely saturate the material during the measurement (due to the fact that h_p values have been fixed for all temperatures). Therefore, the observed deviation could also be explained by the fact that the identified anhysteretic curve M_{an} may be less accurate. As one could expect, the NRMSE decreases as the number of cells N, used to model the material, increases. It is observed that three cells are generally enough to obtain an optimal result, in that a higher number of cells does not reduces significantly the NRMSE.

4.1 Temperature-dependent extension

In practical applications, engineers need to predict the continuous distribution $\omega(\kappa)$ curves at any temperature and/or directly a discretized approximation (ω_k, κ^k).

4.1.1 Continuous $\omega(\kappa|T)$ curves interpolation

In order to assess the robustness of our approach, we have performed a cross-validation by comparing the original functions $\omega(\kappa|T)$ obtained for all available temperatures with interpolated curves obtained by using only half of the dataset. Namely, we have interpolated the distribution by having available only $\omega(\kappa|T)$ for a few temperatures (T = 223 K, 273 K, 323 K, 373 K and 448 K) and tried to reconstruct the five remaining curves (T = 248 K, 293 K, 348 K, 398 K, 423 K). Figure 10 shows the original curves (full lines), obtained by the identification method, and the new computed ones. The interpolated and original curves are in good agreement. This suggests that the model could have been identified by using a reduced set of measurements.

4.1.2 Discrete (ω_k, κ^k) sets function of temperature

A first variation law of parameters in function of temperature is proposed. The continuous distributions $\omega(\kappa|T)$ have been discretized in $N = 3$ cells, thus achieving discrete parameters $(\omega_k(T), \kappa^k(T))_{k=1,\dots,N}$, with temperature T ranging from 223 K to 448 K. As for parameters ω_k, the same property $\sum_{k=1}^{N} \omega_k = 1$ must hold at any temperature. Parameters κ^k are related to a local pinning force or a local coercive field. Therefore the variations of $(\omega_k(T), \kappa^k(T))_{k=1\dots N}$ as a function of temperature T could be obtained by the knowledge of the macroscopic coercive field $h_c(T)$, which has already been measured. More precisely, we hypothesise that, at any temperature,

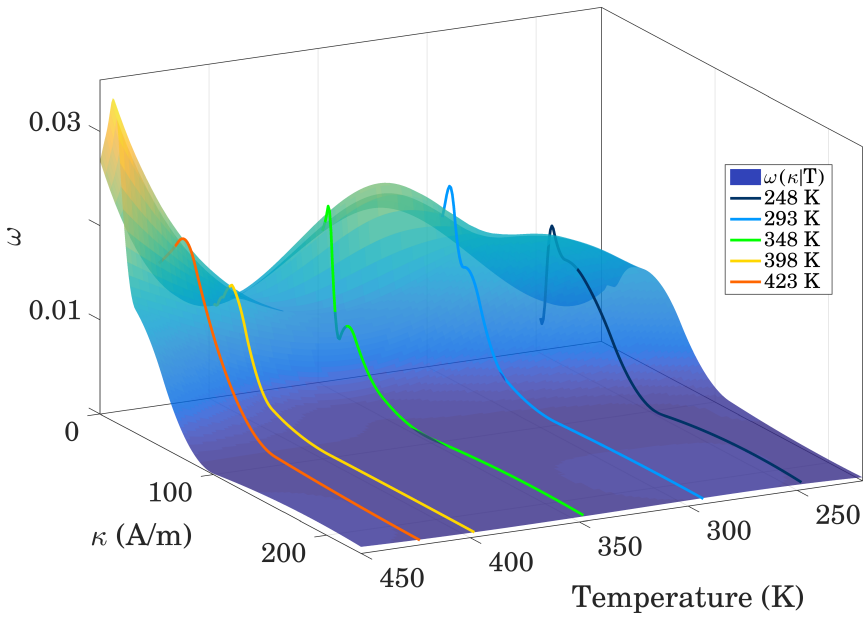

Figure 10: Reconstructed continuous distributions $\omega(\kappa|T)$ and original ones (248 K, 293 K, 348 K, 398 K, 423 K, in full lines).

the products $\omega_k(T) \cdot \kappa^k(T)$ rescale as:

$$\frac{\omega_k(T) \cdot \kappa^k(T)}{\omega_k(T_0) \cdot \kappa^k(T_0)} = \frac{h_c(T)}{h_c(T_0)} \tag{24}$$

in which the ratio is known for a reference temperature T_0. Remark that this is consistent with [Sixdenier and Scorretti, 2018].

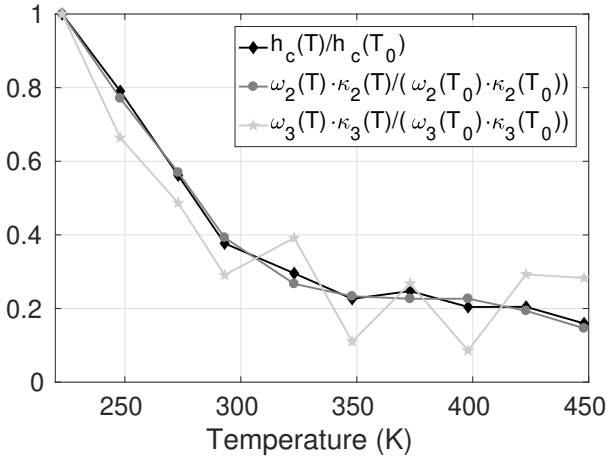

Figure 11: Variation law of parameters with temperature ($T_0 = 223$ K).

Figure 11 shows the curves of (24) for the second and third cell. The first cell $k = 1$ is not represented, since the constraint $\kappa^1 = 0$ is imposed (cf. equation 16), hence (24)

is meaningless. Moreover, κ^1 takes into account the reversible part of the applied field and thus it is not related to the coercive field. Concerning the two irreversible cells, there is a fairly good agreement between the rescaled product of parameters for $k = 2$ and the coercive field. The third cell shows the same trend, but it may be noted the presence of erratic behaviour starting from $T = 293$ K. The same trend is observed for cells of order higher than 3 but with a much more erratic behaviour (not shown). A possible explanation is that starting from $k \geq 4$ the effect of cells is negligible (Fig. 9a), henceforth the parameters of these cells cannot be identified accurately (Table 2).

Therefore, EB models identified at a reference temperature could be used to simulate the behaviour of magnetic materials at other temperatures, at the price of a few measurements to be performed in the desired range of temperature.

5 Conclusions and perspectives

In this paper the Energy-Based hysteresis model has first been analyzed under various magnetization waveforms, and at different temperatures. Globally, results of measured and simulated hysteresis loops are in good agreement at any temperature, and reveal that the identification strategy used to obtain the model parameters is robust and stable, as the parameters identified by simple excitation waveforms can be used to simulate hysteresis loops subject to complex magnetization waveforms.

An extension to the existing EB model has then been proposed, so as to take into account the effect of temperature with only a few measurements, based on a 2D interpolation. A scaling law of the model parameters (ω_k, κ^k) with the temperature has been suggested and partially validated. This constitutes a first step towards predicting hysteresis loops for complex signals and for any temperature falling in the range of available measurements.

However, a considerable amount of work has to be done, on one hand in order to confirm the obtained results and to obtain a better physical rationale which explains the observed trends. On the other hand, methods to predict the behaviour of materials as a function of temperature are valuable tools for engineers. A possible way to obtain this information could be microscopic imaging. In fact, it has been reported in literature [Mager, 1952], [Adler and Pfeiffer, 1974], [Landgraf et al., 2011] that the coercive field is inversely proportional to grain size. Therefore the existence of a possible link between grain size, pinning force distribution and temperature deserves to be investigated.

The proposed approach has currently only been tested with a single material. Future work will be dedicated to evaluating its validity with different materials, as well as

Table 2: Discrete parameters ω_k, κ^k for each temperature, where $k = 1, ..., N$.

	$N=2$		$N=3$		$N=4$		$N=5$	
	ω_k	κ^k	ω_k	κ^k	ω_k	κ^k	ω_k	κ^k
$T = 223$ K	0.3329	0.0000	0.2886	0.0000	0.2871	0.0000	0.2880	0.0000
	0.6670	121.6793	0.6571	40.6363	0.5611	32.0651	0.5512	31.2924
			0.0542	156.5175	0.1276	81.8019	0.1281	78.0576
					0.0241	189.431	0.0326	130.6511
							$2.31e^{-7}$	2294424.8
$T = 248$ K	0.4064	0.0000	0.3284	0.0000	0.3250	0.0000	0.3334	0.0000
	0.5936	120.4370	0.6284	32.8608	0.5149	25.5380	0.0227	2.6633
			0.0432	145.8048	0.1445	63.9543	0.4705	27.8393
					0.0156	147.8423	0.1565	62.3466
							0.0167	147.1808
$T = 273$ K	0.4953	0.0000	0.3758	0.0000	0.3778	0.0000	0.3691	0.0000
	0.5047	120.4085	0.5923	26.6819	0.5938	27.0429	0.4235	2.6633
			0.0319	141.2010	0.0284	143.8204	0.1376	27.8393
					$7.539e^{-7}$	3423.9374	0.0698	62.3466
							$1.046e^{-7}$	108.1089
$T = 293$ K	0.6120	0.0000	0.4469	0.0000	0.4483	0.0000	0.4342	0.0000
	0.3879	119.6603	0.5308	21.3301	0.5310	21.4869	0.4138	125.5438
			0.0222	125.5747	0.0207	125.5438	0.1497	27.8393
					$2.064e^{-7}$	69035.7289	0.0022	115.9689
							$2.486e^{-6}$	322.3601
$T = 323$ K	0.7183	0.0000	0.5488	0.0000	0.5264	0.0000	0.5272	0.0000
	0.2817	118.2481	0.4195	18.4937	0.3086	9.6997	0.3136	10.0647
			0.0316	120.3354	0.1509	33.5657	0.1458	34.0267
					0.0142	129.6345	0.01335	129.9505
							$9.495e^{-6}$	408.6364
$T = 348$ K	0.7908	0.0000	0.6513	0.0000	0.6513	0.0000	0.6183	0.0000
	0.2091	117.6531	0.3382	20.2308	0.3382	20.2323	0.2204	7.6453
			0.0106	102.2365	0.0106	102.0321	0.1607	32.6415
					$1.976e^{-6}$	707.9873	$1.0186e^{-6}$	$-$ 115789.78
							0.0007	127.2204
$T = 373$ K	0.7857	0.0000	0.6375	0.0000	0.6265	0.0000	0.6383	0.0000
	0.2143	117.9743	0.3414	18.7272	0.2682	11.9799	0.3376	18.3745
			0.0211	119.8614	0.0937	36.5363	0.0238	85.0523
					0.012	126.3739	$1.867e^{-6}$	16163.72
							0.0003	558.7124
$T = 398$ K	0.7693	0.0000	0.5614	0.0000	0.5613	0.0000	0.5370	0.0000
	0.2307	118.7189	0.4308	15.266	0.4307	15.2648	0.3187	8.3228
			0.0078	105.7655	0.0079	106.0202	0.1429	28.7854
					$5.6404e^{-7}$	2906.27	$7.7661e^{-7}$	70850.24
							0.0012	298.5686
$T = 423$ K	0.7879	0.0000	0.5803	0.0000	0.5722	0.0000	0.5722	0.0000
	0.2120	119.6366	0.3993	13.5199	0.3308	10.2054	0.3320	10.2346
			0.0204	133.4828	0.0867	27.9707	0.0856	28.1412
					0.0102	143.5946	0.0100	144.3593
							$7.0364e^{-7}$	2933.352
$T = 448$ K	0.8148	0.0000	0.5643	0.0000	0.5445	0.0000	0.5445	0.0000
	0.1852	119.5290	0.4146	10.0618	0.3292	5.9373	0.3306	5.9669
			0.021	128.0142	0.1152	20.5528	0.1139	20.7185
					0.0109	145.5584	0.0107	146.3299
							$4.0234e^{-7}$	3418.89

integrating it in Finite Element software to provide an accurate mapping of magnetic losses for practical electrotechnical applications.

References

[Fer, 2013] (2013). Soft Ferrites and Accessories - Data Handbook. [Online]. Available: https://elnamagnetics.com/wp-content/uploads/catalogs/Ferroxcube/catalog.pdf.

[Adler and Pfeiffer, 1974] Adler, E. and Pfeiffer, H. (1974). The influence of grain size and impurities on the magnetic properties of the soft magnetic alloy 47.5% NiFe. *IEEE Trans. Magn.*, 10(2):172–174.

[Benabou et al., 2008] Benabou, A., Leite, J., Clnet, S., Simo, C., and Sadowski, N. (2008). Minor loops modelling with a modified Jiles–Atherton model and comparison with the Preisach model. *Journal of Magnetism and Magnetic Materials*, 320(20):e1034–e1038.

[Bergqvist, 1997] Bergqvist, A. (1997). Magnetic vector hysteresis model with dry friction-like pinning. Physica B(233):342–347.

[Bergqvist et al., 2014] Bergqvist, A., Lin, D., and Zhou, P. (2014). Temperature-dependent vector hysteresis model for permanent magnets. 50(2):345–348.

[Bergqvist et al., 1997] Bergqvist, A., Lundgren, A., and Engdahl, G. (1997). Experimental testing of an anisotropic vector hysteresis model. *IEEE Transactions on Magnetics*, 33(5):4152–4154.

[Cass et al., 2007] Cass, C., Wang, Y., Burgos, R., Chow, T. P., Wang, F., and Boroyevich, D. (2007). Evaluation of SiC JFETs for a Three-Phase Current-Source Rectifier with High Switching Frequency. *Twenty Second Annual IEEE Applied Power Electronics Conference and Exposition (APEC).*

[François-Lavet et al., 2011] François-Lavet, V., Henrotte, F., Stainier, L., Noels, L., and Geuzaine, C. (2011). Vectorial Incremental Nonconservative Consistent Hysteresis model. *ACOMEN.*

[Henrotte et al., 2006] Henrotte, F., Nicolet, A., and Hameyer, K. (2006). An energy-based vector hysteresis model for ferromagnetic materials. *COMPEL - The International Journal of Computations and Mathematics in Electrical and Electronic Engineering*, 25(1):71–80.

[Henrotte et al., 2014] Henrotte, F., Steentjes, S., Hameyer, K., and Geuzaine, C. (2014). Iron Loss Calculation in Steel Laminations at High Frequencies. *IEEE Transactions on Magnetics*, 50(2):333–336.

[Jacques et al., 2018] Jacques, K., Steentjes, S., Henrotte, F., Geuzaine, C., and Hameyer, K. (2018). Representation of microstructural features and magnetic anisotropy of electrical steels in an energy-based vector hysteresis model. *AIP Advances*, 8(4):047602.

[Jiles and Atherton, 1986] Jiles, D. C. and Atherton, D. L. (1986). Theory of ferromagnetic hysteresis. *Journal of Magnetism and Magnetic Materials*, 61:48–60.

[Landgraf et al., 2011] Landgraf, F. J. G., da Silveira, J. R. F., and Rodrigues-Jr., D. (2011). Determining the effect of grain size and maximum induction upon coercive field of electrical steels. *Journal of Magnetism and Magnetic Materials*, 323(18-19):2335–2339.

[Mager, 1952] Mager, A. (1952). About the influence of grain size on the coercivity. *Ann. Phys. Leipzig*, 446:15–16.

[Petrun et al., 2017] Petrun, M., Steentjes, S., Hameyer, K., and Dolinar, D. (2017). Comparison of static hysteresis models subject to arbitrary magnetization waveforms. *COMPEL - The International Journal of Computations and Mathematics in Electrical and Electronic Engineering*, 36(3):774–790.

[Preisach, 1935] Preisach, F. (1935). Über die magnetische nachwirkung. *Zeitschrift für Physik*, 94(5):277–302.

[Preisach, 2017] Preisach, F. (2017). On the Magnetic Aftereffect. *IEEE Transactions on Magnetics*, 53(3):1–11.

[Raghavender et al., 2010] Raghavender, A., Zadro, K., Pajic, D., Skoko, Z., and Bilikov, N. (2010). Effect of grain size on the Néel temperature of nanocrystalline nickel ferrite. *Materials Letters*, 64(10):1144–1146.

[Raghunathan et al., 2010] Raghunathan, A., Melikhov, Y., Snyder, J. E., and Jiles, D. C. (2010). Theoretical Model of Temperature Dependence of Hysteresis Based on Mean Field Theory. *IEEE Trans. Magn.*, 46(6):1507–1510.

[Rayleigh, 1887] Rayleigh, L. (1887). XXV. Notes on electricity and magnetism. iii. On the behaviour of iron and steel under the operation of feeble magnetic forces. *The London, Edinburgh, and Dublin Philosophical Magazine and Journal of Science*, 23(142):225–245.

[Sixdenier and Scorretti, 2018] Sixdenier, F. and Scorretti, R. (2018). Numerical model of static hysteresis taking into account temperature: Static hysteresis taking into account temperature. *International Journal of Numerical Modelling: Electronic Networks, Devices and Fields*, 31(2):e2221.

[Song and Roshko, 2000] Song, T. and Roshko, R. (2000). Preisach model for systems of interacting superparamagnetic particles. *IEEE Transactions on Magnetics*, 36(1):223–230.

[Stancu and Spinu, 1998] Stancu, A. and Spinu, L. (1998). Temperature- and time-dependent Preisach model for a Stoner–Wohlfarth particle system. *IEEE Transactions on Magnetics*, 34(6):3867–3875.

[Zirka et al., 2012] Zirka, S. E., Moroz, Y. I., Harrison, R. G., and Chwastek, K. (2012). On physical aspects of the Jiles-Atherton hysteresis models. *Journal of Applied Physics*, 112(4).